Environmental Research 231 (2023) 116250

Contents lists available at ScienceDirect

Environmental Research

journal homepage: www.elsevier.com/locate/envres

Geochemical and morphological characterization of particles originating from tunnel construction

Emelie Forsman [a,b,*], Lene Sørlie Heier [c], Hans-Christian Teien [d], Ole Christian Lind [d], Per Hagelia [c], Sondre Meland [a,b]

[a] Norwegian Institute for Water Research, Oslo, Norway
[b] Norwegian University of Life Sciences, Faculty of Environmental Sciences and Natural Resource Management, Ås, Norway
[c] Norwegian Public Roads Administration, Construction, Lillehammer, Norway
[d] Norwegian University of Life Sciences, Faculty of Environmental Sciences and Natural Resource Management, Centre of Environmental Radioactivity, Ås, Norway

ARTICLE INFO

Handling Editor: Aijie Wang

Keywords:
Tunnel drilling and blasting
Shape analysis
Particle analysis
Granite-gneiss terrain

ABSTRACT

Rock particles from drilling and blasting during tunnel construction (DB particles) are released to the aquatic environment where they may cause negative toxicological and ecological effects. However, there exists little research on the difference in morphology and structure of these particles. Despite this DB particles are assumed to be sharper and more angular than naturally eroded particles (NE particles), and in consequence cause greater mechanical abrasion to biota. Moreover, morphology of DB particles is assumed to depend on geology, thus depending on where construction takes place different morphologies may be emitted. The objectives in the current study were to investigate the morphological differences between DB and NE particles, and the influence of mineral and elemental content on DB particles. Particle geochemistry and morphology were characterized by inductively coupled plasma mass spectrometry, micro-X-ray fluorescence, X-ray diffraction, environmental scanning electron microscope interfaced with energy dispersive X-ray, stereo microscope, dynamic image analysis and coulter counter. DB particles (61–91% < 63 μm) collected from five different tunnel construction locations in Norway were 8–15% more elongated (lower aspect ratio) than NE particles from river water and sediments, although their angularity was similar (solidity; diff 0.3–0.8%). Despite distinct mineral and elemental characteristics between tunnel construction locations, DB morphology was not explained by geochemical content since only 2–2.1% of the variance was explained. This suggests that particle formation mechanisms during drilling and blasting are more influential of morphology than mineralogy, when working in granite-gneiss terrain. When tunnelling in granite-gneiss terrain, particles with greater elongation than natural particles may enter aquatic systems.

1. Introduction

Globally, road and tunnel networks are continuously expanding to maintain a functioning infrastructure (Meijer et al., 2018). However, despite its benefits for socio-economic development, the construction of roads and tunnels poses various environmental hazards to surrounding ecosystems (Angermeier et al., 2004; Lundy et al., 2016; Mooselu et al., 2022). Drilling and blasting of bedrock, which are primary activities during road and tunnel construction, emit various pollutants to aquatic environments (Hindar and Nordstrom, 2015; Hjulstad, 2015; Pabst et al., 2015; Vikan and Meland, 2013; Wærsted, 2019). Among these pollutants, particles have been poorly investigated, particularly morphological and geochemical characteristics (Kaegi, 2004; Pabst et al., 2015; Roseth et al., 2021; Åstebøl et al., 2011).

During drilling and blasting of bedrock in road and tunnel construction, large numbers of rock particles are produced (geological source; henceforth referred to as DB particles). Since DB particles are released into aquatic recipients where the load of naturally eroded particles (henceforth referred to as NE particles) may vary enormously with season, weather and location, the difference between the two particle types is of particular interest during environmental risk assessment related to road and tunnel projects (Pabst et al., 2015; Roseth et al., 2021). Because newly produced DB particles are believed to be more angular, rough, elongated and needle-like in morphology (Pabst et al.,

* Corresponding author. Norwegian Institute for Water Research, Oslo, Norway.
E-mail address: emelie.forsman@niva.no (E. Forsman).

https://doi.org/10.1016/j.envres.2023.116250
Received 11 November 2022; Received in revised form 12 May 2023; Accepted 26 May 2023
Available online 1 June 2023

2015; Roseth et al., 2021; Åstebøl et al., 2011) compared to NE particles owing to the differences in origin and erosion processes (Pabst et al., 2015). Due to the believed differences in morphology, it is also assumed that DB particles cause greater abrasion and therefore pose a greater hazard to aquatic wildlife despite very little primary scientific evidence (Hessen et al., 1989; Jacobsen et al., 1987; Pabst et al., 2015). However, very few studies exist on particle morphology related to different construction activities (Cepuritis et al., 2014; Kaegi, 2004; Little et al., 2015; Roseth et al., 2021; Xing et al., 2021; Yang et al., 2019). Nonetheless, it's highly likely that DB and NE particles differ in morphology, however the understanding on how and to what degree they differ, is lacking (Roseth et al., 2021).

Besides source and erosion history affecting morphology, mineralogy also effects particle morphology (e.g., Xing et al., 2021; Åkesson et al., 2001). For example, asbestos minerals or other fibrous minerals release needle-like fibrous particles (Gualtieri, 2020; Pabst et al., 2015), while plagioclase and K-feldspar have a tendency for rectangular crystalline shapes (Lois-Morales et al., 2022). However, limited research exists on how and to what extent mineralogy influences the morphology of DB particles from tunnels (Roseth et al., 2021). Thus, depending on the underlying geology of the current road and tunnel project, newly produced DB particles released into aquatic ecosystems may contain a plethora of irregular particles varying within and between projects. Hence, to better understand the possible ecological and toxicological implications of particle emission from tunnelling, both morphological and geochemical characterization of tunnel particles are needed (Roseth et al., 2021).

In the current study, the first aim was to characterize and evaluate the influence of mineral composition and elemental content on morphology of DB particles from several tunnelling construction sites in Norway, with the hypothesis that geology affect morphology of particles from drilling and blasting. The second aim was to address the knowledge gaps concerning differences in morphology between DB particles from various tunnel construction sites in Norway and NE particles from river water and sediments (as a reference), with the hypothesis that DB particles are more elongated and angular than NE particles.

2. Materials and methods

2.1. Site location and sample collection

Tunnelling slurry, a semi-liquid mixture of fine DB particles suspended in water, was collected from five ongoing tunnel construction projects (henceforth referred to as Rafoss, Stryn, Verket, Årdal and Åseral; Fig. 1 & SI-A; Tab. S1) in southern and western Norway during the spring of 2020 (SI–B). Tunnelling slurries were collected from inside the tunnel and from sedimentation containers located outside the tunnel depending on safety and covid-19 related restrictions in the sampled tunnel (SI-A Table S1). In addition, NE particles were collected from two sites for comparison with DB particles. Surface sediment samples were collected from the river Vikka (Norway), and from a stream, Ravinebekken (Norway), at two timepoints (22nd of October after a heavy rainfall and 2nd of November after a dry period) by the Norwegian Water Resources and Energy Directive. Both Vikka and Ravinebekken were unaffected by construction work.

Tunnelling slurries were collected at depths of 0–25 cm with a small Van Veen grab or a spade, into rinsed 11 L plastic buckets. Slurry was collected randomly at the site and pooled to an approximate fresh weight of 30–50 kg, homogenized by stirring, and stored cool (4 °C) until further treatment. Surface sediments at Vikka were randomly collected within a meter radius, down to 1 cm, with a stainless-steel spoon into rinsed plastic bottles and surface water from Ravinebekken was directly sampled into rinsed plastic bottles and stored cool (4 °C) until further analysis.

2.2. Sample preparation

Prior to morphological and geochemical analyses, the tunnelling slurries were homogenized by stirring, and then sieved through a 2 mm sieve (henceforth referred to as bulk sample). Accumulated particles larger than 2 mm were discarded. Next, two subsamples were collected; one sample was kept as a bulk sample while the other sample was wet sieved for size fractionation.

Wet sieving of DB particles was carried out following Kettler et al. (2001) with a few adjustments. In brief, deionized water and wet tunnelling slurry (~3.3 g/mL) were ultrasonicated for 5 min to prevent aggregation. The slurry suspensions were sieved through consecutive sieves (cell size of 15, 20, 63, 150, 200, 400, 630 μm) with deionized water and the suspension containing sizes smaller than 15 μm were collected into a glass beaker. Accumulated particles on the sieves and in the glass beaker were retrieved and stored cool (4 °C) until analysis. In addition, representative subsamples were collected from each fraction, freeze-dried, and weighed to calculate weight proportional size fractions.

Subsamples from bulk samples and, for certain analyses, size fractions (which fractions were used are specified in the following sections) of tunnelling slurries were analysed for mineral composition with X-ray diffraction (XRD), element concentrations with inductively coupled plasma mass spectroscopy (ICP-MS) and element composition with micro-X-ray fluorescence (μXRF). Element-specific morphological analysis was performed with static image analysis (SIA) using environmental scanning electron microscopy coupled with energy dispersive X-ray spectroscopy (ESEM-EDX) and stereo microscopy (SM). In addition, quantitative morphological and size distribution analysis were performed with dynamic image analysis (DIA) and laser diffraction. Vikka surface sediment and two water samples from Ravinebekken were only analysed for quantitative particle morphology by DIA.

2.3. Size fraction distribution with laser diffraction

Particle size distribution (0.4–2000 μm) in bulk samples of tunnelling slurries was measured by laser diffraction using a Beckman Coulter LS 13,320 (Pye and Blott, 2004). Deionized water (300 mL; 0.2 μm filtered), wet bulk slurry (~3 g) and dispersant (~15% 0.05 M tetrasodium pyrophosphate) were mixed and ultrasonicated for 5 min to prevent aggregation. The suspensions were stirred with a magnetic stirrer while 50–140 mL suspension were taken with a syringe and added to the Beckman Coulter LS 13,320 until reaching 7–12% obscuring. All samples were analysed three times, with a pump speed of 45%, without polarized intensity differential scattering, but including automatic rinsing between samples, and Fraunhofers model as the optical model (refraction index 1.333 and absorption index 0.1).

2.4. Mineralogy with XRD

Minerals in bulk samples and size fractions (15–20 μm, 20–63 μm, 63–150 μm, 150–200 μm for Verket, Årdal and Stryn, in addition 200–400 μm for Rafoss and Åseral; SI-A Table S2) of tunnelling slurries were identified by X-ray diffraction (XRD; Bruker, D8 Advance) equipped with a Co X-ray tube with a wavelength of 1.79 Å at Norwegian University of Science and Technology (NTNU). Prior to analysis, wet samples were ground down to 10 μm with ethanol and mounted onto a sample holder creating a flat upper surface and analysed by rotation (60 rpm) with an angle between 3 and 80° 2-theta scale with step size 0.01° per second. The mineral phases were identified by using the program Diffrac. eva which uses the mineral database PDF 4+. To quantify mineral content, the program Topas was used, which is based on the Rietveld method (Rietveld, 2014).

2.5. Element characteristics with ICP-MS and μXRF

Concentrations of elements in freeze-dried and digested bulk samples and size fractions (15–20 μm, 20–63 μm, 63–150 μm, 150–200 μm for Verket, Årdal and Stryn, in addition 200–400 μm for Rafoss and Åseral; SI-A Table S3) of tunnelling slurries (~0.02–0.2 g) were analysed with ICP-MS (Agilent 8800 and 8900). Prior to analysis, parallel aliquots of both bulk samples and size fractions were dissolved in a microwave assisted (Milestone, Ultraclave IV) acid digestion (260 °C for 50 min) using two different acid treatments on each parallel (~23 mL/g). The first acid treatment was a mixture of ultrapure nitric acid (HNO_3) 65% and ultrapure hydrofluoric (HF) acid 48% (5:1) and the second acid treatment was ultrapure HNO_3 65%. Silicon was not detected in ICP-MS because of instrumental limitations and was instead estimated with μXRF (SI-A Table S4), as explained in SI–B.

2.6. Morphological analysis

Morphological analysis of particles was performed with SIA (DB particles) and DIA (DB and NE particles). For detailed information about analysis of particle morphology, consult SI–B. In the current study, morphological descriptors for particles included form, angularity, and surface texture which were measured with the morphology parameters aspect ratio (AR), solidity (SLD) and convexity (CVX), respectively (Barrett, 1981; Liu et al., 2015; Maroof et al., 2020, Fig. 2; Table 1). Form describes whether the particle is circular (1) or elongated (0), angularity describes whether the projections protruding from the particles' surface are smooth (1) or angular (0), and surface texture describes the relative roughness (less rough: 1, rougher: 0) of the particle's surface on a microscale (Liu et al., 2015; Maroof et al., 2020, Fig. 2). Additionally, diameter of a circle of equal projection area

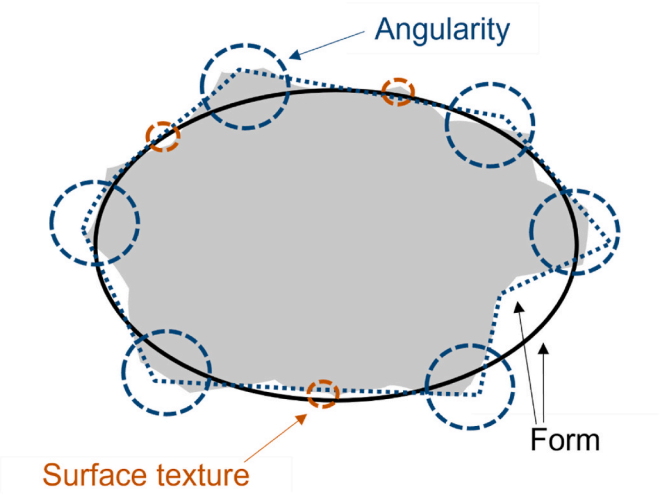

Fig. 2. Figure adopted from Barrett (1981). A particle (grey) with its form (black solid line, two approximations given), angularity (blue dashed circles and blue dashed line) and surface texture (red dashed circles) shown.

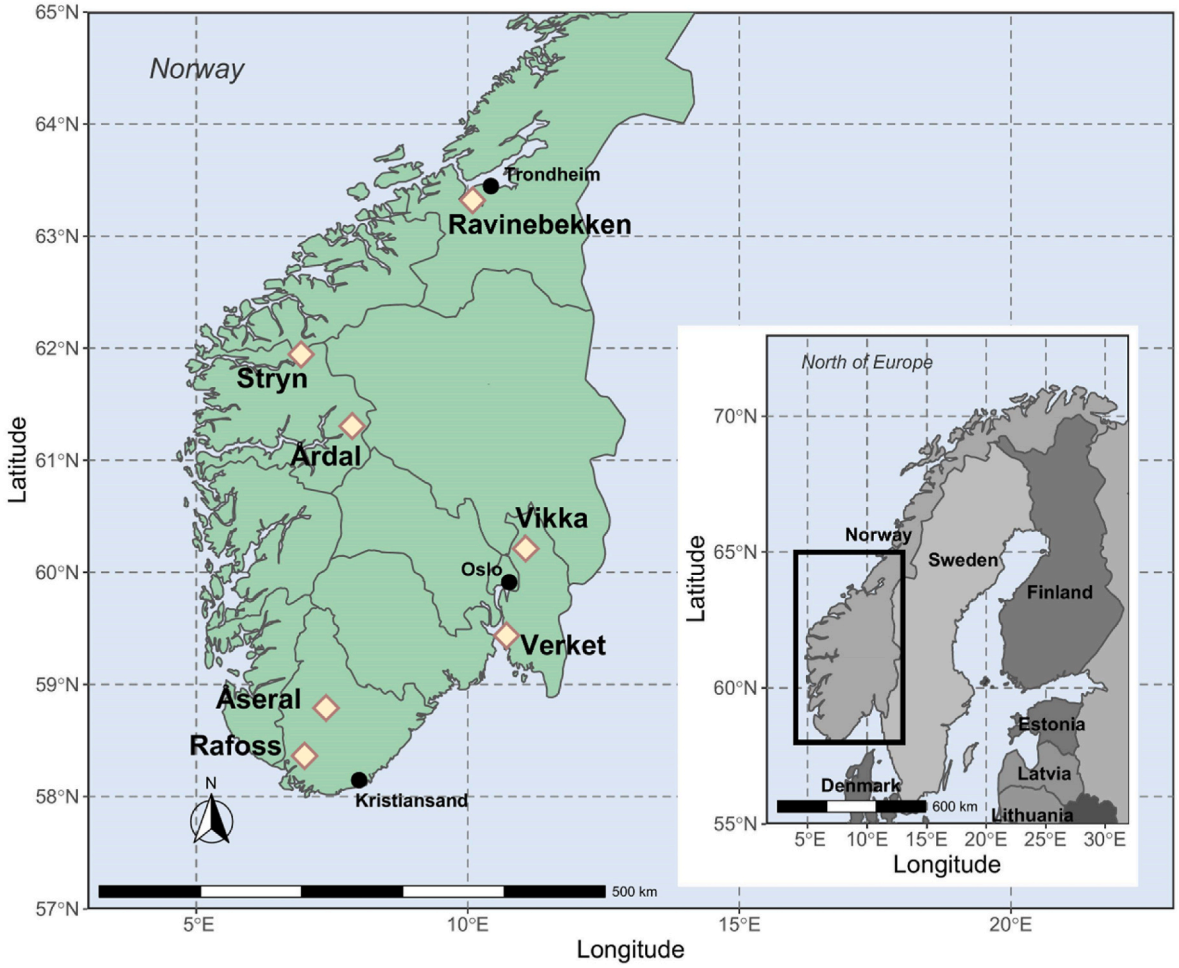

Fig. 1. Map over Norway with the field sites (Tunnel construction sites: Stryn, Rafoss, Verket, Årdal and Åseral; Rivers: Ravinebekken and Vikka) marked in yellow and North of Europe (right bottom corner; 'rnaturalearth' package (South, 2017)).

Table 1
Particle size measures and morphology parameters used in Static Image Analysis (SIA) and Dynamic Image Analysis (DIA) in the current study.

Size measurement	Abbreviation	Definition			DIA vs SIA
Minimum Feret diameter	Fmin	Shortest distance between two lines tangential to the particle outline			DIA, SIA
Maximum Feret diameter	Fmax	Maximum distance between two parallel lines tangential to the particle outline			DIA, SIA
Area of the particle	A_p	Area of the pixels in the particle			DIA, SIA
Area of the convex hull	A_{ch}	Area of the pixels in the convex hull			DIA, SIA
Perimeter of the particle	P_p	Length of the outside boundary of the particle			Only SIA
Perimeter of the convex hull	P_{ch}	Length of the outside boundary of the convex hull			Only SIA
Diameter of the circle of equal projection area	D_{EQPC}	Diameter of the circle having the same area as the particle's projection			DIA, SIA
Morphology parameters	Abbreviation	Formula	Sensitivity to	Reference	DIA vs SIA
Aspect ratio	AR	F_{min}/F_{max}	Form (Fig. 1)	(Liu et al., 2015; Mazzoli and Favoni, 2012; Mazzoli and Moriconi, 2014)	Same calculation
Solidity	SLD	A_p/A_{ch}	Angularity (morphological roughness; Fig. 1)	(Cioni et al., 2014; Leibrandt and Le Pennec, 2015; Liu et al., 2015)	Same calculation[a]
Convexity	CVX	P_{ch}/P_p	Surface texture (textual roughness; Fig. 1)	(Leibrandt and Le Pennec, 2015; Liu et al., 2015)	Not calculated in DIA
Fibers		$\geq 3\ F_{max}/F_{min} \ni >> 5\ \mu m\ F_{max}$		WHO (1985)	Same calculation

[a] Named convexity in the QICPIC software.

(EQPC), pixel density and if particles were fibrous or not (WHO, 1985) were calculated (Table 1).

2.6.1. Static image analysis (SIA) with ESEM-EDX and stereo microscope

Morphological parameters of DB particles were measured for size fractions <20 μm (<15 μm and 15–20 μm were combined), 20–63 μm, 63–150 μm, 150–200 μm for Verket, Årdal and Stryn, and in addition 200–400 μm and 400–630 μm for Rafoss and Åseral with SIA (SI-A Table S5). Particle sizes between 0 and 200 μm were imaged using an Environmental Scanning Electron Microscope (ESEM; Zeiss EVO 50 variable pressure 38–50 Pa, 30 kV accelerating voltage, 7–9 mm working distance; 0.34–17 pixels/μm; SI-A Tab. S5 & SI-B) in backscatter (BEI) electron imaging mode. Particle sizes between 200 and 630 μm were imaged using a stereo microscope (SM; ZEISS Axio Zoom V16; 0.09–0.17 pixels/μm; SI-A Tab. S5 & SI-B). To minimize systematic bias from size-dependent morphologies, a constant pixel density range of 750–4000 pixels per particle (pxl/p; Liu et al., 2015) was used by adjusting the magnification (SI-A Tab. S6 & SI-BS).

Sample preparations of DB particle size fractions <63 μm followed Mazzoli and Favoni (2012). In brief, homogenized, freeze-dried and separated size fractions were mixed with deionized water (0.05–0.125 mg/mL) and ultrasonicated for 5 min. A subsample (5 mL) was collected from stirred suspensions and then vacuum filtered onto a 0.4 μm filter (Isopore Membrane Filters, Millipore) and dried. Next, the membrane was attached to carbon double-faced sticky tape and mounted onto aluminium stubs. DB particle size fractions >63 μm were analysed according to Liu et al. (2015). In brief, homogenized and freeze-dried size fractions of tunnelling slurries were mounted directly onto the carbon double-faced sticky tape on aluminium stubs by sprinkling a small subsample over the tape while applying compressed air to avoid particle aggregation. The aluminium stubs with particles were then used in ESEM and SM to acquire images.

When imaging, random positions on the stub were chosen, suitable magnification was set, and an image was captured. This was repeated until 10–20 particles per size fraction were attained. The imaged particles were also subjected to element identification (ESEM-EDX) and standard-less semi-quantification using the integrated Oxford Instruments INCA 5.05 software (Oxford Instruments, Oxford, UK) with a Si (Li) detector by performing point measurements (spatial resolution of ~1 μm) at the center of the particles using an acceleration voltage of 30 kV (SI-A Table S7). Dead times were ~30%. Elements were normalized to mass concentration in %.

All images from ESEM and SM were processed in ImageJ (National Institute of Health (NIH), US, https://imagej.nih.gov/ij/). The procedure in ImageJ followed Liu et al. (2015), with a few adjustments described in the supporting material (SI–B). From ImageJ, particle size, morphological measurements described in Table 1 were obtained. These measurements were exported and further analysed in R software (version 4.1.2, R Core Team, 2021).

2.6.2. Dynamic image analysis (DIA)

Morphological parameters of DB particles were measured for size fractions 15–63 μm (15–20 μm and 20–63 μm combined) and 63–200 μm (63–150 μm and 150–200 μm) for Rafoss, Stryn, Verket, Årdal and Åseral. In addition, 200–400 μm were measured for Rafoss and Åseral and 15–63 μm for NE particles. Morphological parameters for these subsamples were measured with a QICPIC imaging system connected to a Lixell using wet dispersion (Sympatec GmBH) at Sympatec (Shang et al., 2017; Sun et al., 2019b). To minimize systematic bias from size-dependent morphologies (Altuhafi et al., 2013; Sun et al., 2019a) a constant pixel density range of 585 to 10,299 pxl/p was used by adjusting the imaging lenses to the size fractions (0.2, 0.6 and 1.8 pixels/μm for the M7, M5 and M3 lens; SI-A Table S8). These imaging lenses cannot offer the same pixel density range as SIA, and consequently the minimum and maximum sized particles were more restricted for DIA (15 μm and 400 μm, respectively) than SIA.

Prior to analysis, samples of freeze-dried size fractions (weight proportional to size distribution in the bulk sample; 0.5–7.5 mg/mL) of tunnelling slurry and Vikka surface sediment (5 mg/mL) were dispersed in deionized water. These suspensions and Ravinebekken water samples (400 mL) were added directly to the QICPIC imaging system for analysis. The sample passed through a flow cuvette (depth 0.5–2 mm) and a high-speed camera obtained the images of the particles (2D projections) with a frame rate of 70 Hz per second for 60 s.

All binary images of projection particles from the QICPIC imaging system were processed in QICPIC Dynamic Image Analysis application software (Sympatec GmBH), and size and morphology measurements were exported and further analysed in R software (version 4.1.2, R Core Team, 2021). Size and morphology parameters in DIA are the same as for SIA, except for CVX which is not available in the QICPIC software (Table 1).

2.7. Statistics

Quality assurance for laser diffraction, DIA and ICP-MS (including all elements with abbreviations) can be found in SI-A & B. All statistical analyses were performed using the software R (version 4.1.2, R Core Team, 2021) with the α-level set at <0.05 for statistical significance.

Limit of detection (LOD) for XRD was set to <1% (5% LODs, Table S2). Nondetectable values (<LOD) were replaced using a multiplicative lognormal function (multLN) in 'zCompositions' package in R software (Palarea-Albaladejo and Martín-Fernández, 2015). For surface

element detection with ESEM-EDX LOD was set to <0.1% (Newbury and Ritchie, 2013), and no non-detects were found. LOD for element concentrations from ICP-MS was set to three times the standard deviation of the method blanks (5% LODs, SI-A Table S3). Values < LOD were replaced with values between 0 and LOD using a multiple imputation method (assuming a beta distribution; $\alpha = 1$, $\beta = 5$; Baccarelli et al., 2005). Both XRD and ESEM-EDX datasets contain count zeros (Gagnon et al., 2020; Pawlowsky-Glahn and Buccianti, 2011; Quinn et al., 2019; Wheeler et al., 2021) which were replaced with a randomly generated value between 0.1*LOD–LOD (Lubbe et al., 2021).

Morphological differences between locations and size fractions from DIA were investigated with various statistical tests depending on the distribution of residual data and variance which were evaluated with diagnostic plots. One-way analysis of variance (ANOVA) was used for normal residual data with homogenic variance, followed by Tukey's Honest Significant Difference (HSD) post-hoc test. For non-normal residual data and heterogenic variance, Kruskal-Wallis rank sum test was used, followed by Dunn's post-hoc test with Bonferroni correction accounting for multiple testing. Size-dependency between morphology parameters and pixel densities were investigated with Pearson correlations.

Prior to ordination analyses, element concentrations (ng/g dry weight (dw)) from ICP-MS were log transformed ($\log_{10}$ (x+1)). The compositional mineral and surface element data from XRD and ESEM-EDX following replacement of LODs and count zeros, was centered and log-ratio transformed (Aitchison, 1986; Aitchison and Greenacre, 2002) using the function 'clr' in the 'compositions' package in R software (Greenacre, 2018; Van den Boogaart and Tolosana-Delgado, 2013; Wheeler et al., 2021).

Principal component analysis (PCA) was used on the datasets from XRD, ICP-MS and SIA separately to assess the variation in the datasets. Redundancy analysis (RDA) with Monte-Carlo permutation test (999; Oksanen et al., 2017) was used to evaluate if location and size fraction explained the variance in the XRD, ICP-MS and SIA datasets separately. Element concentrations from ICP-MS, mineral composition and surface elemental composition from ESEM-EDX were used in forward model selection (Blanchet et al., 2008) on RDA models with DIA and SIA data, respectively, to evaluate if minerals and elements explained the variance in morphology.

Morphological values (0–1) of AR and SLD were divided into categories with descriptive terms of the morphologies for easier interpretation of the data; "Elongated & Angular" (<AR 0.7 & <SLD 0.85), "Circular & Smooth" (≥AR 0.7 & ≥SLD 0.85), "Elongated & Smooth" (<AR 0.7 & ≥SLD 0.85) and "Circular & Angular" (≥AR 0.7 & <SLD 0.85; Leibrandt and Le Pennec, 2015; SI-A Tables S9 and S10).

3. Results

3.1. Particle size distribution

Size distributions (laser diffraction; Coulter Counter with lower limit of 0.4 μm) of the tunnelling slurries (n = 5) displayed similar distribution patterns (bell shaped; SI-A Fig. S1). The cumulative volume of particles <63 μm ranged from 60.6% (Stryn) to 90.5% (Verket) and under <10 μm ranged from 21% (Stryn) to 59% (Rafoss).

3.2. Mineral composition

Proportions of amphibole, calcite, chlorite, clinozoisite, epidote, k-feldspar, magnetite, mica, plagioclase, pyroxene, quartz, and zeolite were identified in the tunnelling slurries with XRD. Generally, k-feldspar, plagioclase and quartz were the dominant minerals at all tunnelling locations and among the size fractions (mean ± standard deviation; 33 ± 5%, 23 ± 6% and 18 ± 3%; Fig. 3B & SI-A Table S2). The two first axes (PC1 and PC2) summarized 58% of the total variance in a PCA of the mineral data (data not shown). The mineral compositions among the locations were significantly different, and the constraining variable location explained 78% of the variance in the partial RDA (covariable: size fraction, n = 22, p = 0.001, Fig. 3A). Size fraction was not significant. Rafoss and Stryn had higher mineral proportions of plagioclase and pyroxene and less of calcite, while Verket and Åseral exhibited the opposite pattern. Årdal had higher contributions of amphibole and chlorite, and lower contributions of quartz and contained the unique minerals epidote and zeolite (Fig. 3A–B).

3.3. Element concentrations

Based on the ICP-MS analysis, including estimated Si (μXRF), the major elements (>1% dw) among all tunnelling slurries were Al, Ca, Fe, K, Mg, Na, Si and Ti, which together constituted 98 ± 1% dw. Si constituted the greatest proportion (43.4 ± 6% dw) and the remaining elements were divided into minor and trace elements (SI-A Table S3). In a PCA of the element data, PC1 and PC2 summarized 67% of the total variance (data not shown). Element concentrations were significantly different among locations and size fractions which together explained 91% of the constrained variance in the RDA (n = 22, p = 0.001, Fig. 3C). Furthermore, the partial RDA models explained 88% for location (covariable: size fractions, p = 0.001) and 76% for size fraction (covariable: location, p = 0.001).

Higher Na and K concentrations and lower concentrations of most elements (e.g., Si, Fe, Lu, Sc, Yb) at Stryn and Rafoss, drove the separation from Verket and Åseral. Meanwhile, higher concentrations of for instance Al, Co, Cr and lower concentrations of K, Tl and Th, separated Årdal from all other locations (Fig. 3C). Generally, most elements increased along RDA1 and RDA2 alongside decreasing size fractions (Fig. 3C).

3.4. Static image analysis (SIA) combined with particle-specific surface chemistry

Altogether, 222 DB particles were imaged with ESEM and SM, and analysed with ESEM-EDX. Particles ranged from 1.9 to 631 μm with pixel densities between 792-3992 pxl/p (2124 ± 896 pxl/p; SI-A Fig. S2, S3A-B & Tables S5 and S7). No size-dependency were found for AR, SLD, and CVX with pixel density (Pearson correlation; 0.12 (p = 0.07), 0.26 (p < 0.001) and −0.27 (p < 0.001), SI-A Fig. S4).

"Elongated & Angular" particles dominated (51-35%) and AR and SLD overlapped for all tunnelling locations ranging from 0.59 to 0.62 (±0.15–0.18) and 0.82–0.86 (±0.04–0.06), respectively. CVX were close to 1 for all locations 0.94–0.95 (±0.04–0.07), indicating little surface texture roughness (SI-A, Fig. S5A, Table S5). Furthermore, % fiber varied among the locations, with 10.9%, 2.8%, 9.8%, 4.3% and 3.9% for Rafoss, Stryn, Verket, Årdal and Åseral, respectively (SI-A Fig. S5B & Table S5).

In a PCA of the SIA data, PC1 and PC2 summarized 97% of the total variance (SI-A Fig. S6). Furthermore, no surface element detected in ESEM-EDX significantly explained the constrained morphological variance in the SIA dataset analysed with RDA, and thus no element-specific morphologies were found (n = 222, p = 0.231, SI-A Fig. S7).

3.5. Dynamic image analysis (DIA)

Altogether 711,263 DB particles were imaged with DIA. Particles ranged from 15 to 400 μm and had pixel densities between 585-10,299 pxl/p (1933 ± 1504 pxl/p). For NE particles 28,840 particles were imaged with DIA, ranging from 15 to 63 μm with pixel densities between 585-10,289 pxl/p (1469 ± 1351 pxl/p; SI-A Table S8). No size-dependency were found for AR and SLD with pixel density (Pearson Correlation: 0.03 (p < 0.001) and −0.08 (p < 0.001), respectively, SI-A Fig. S8).

"Elongated & Smooth" particles were dominant (51–56%) and AR and SLD overlapped for all DB particles, ranging from 0.58 to 61 (±0.15)

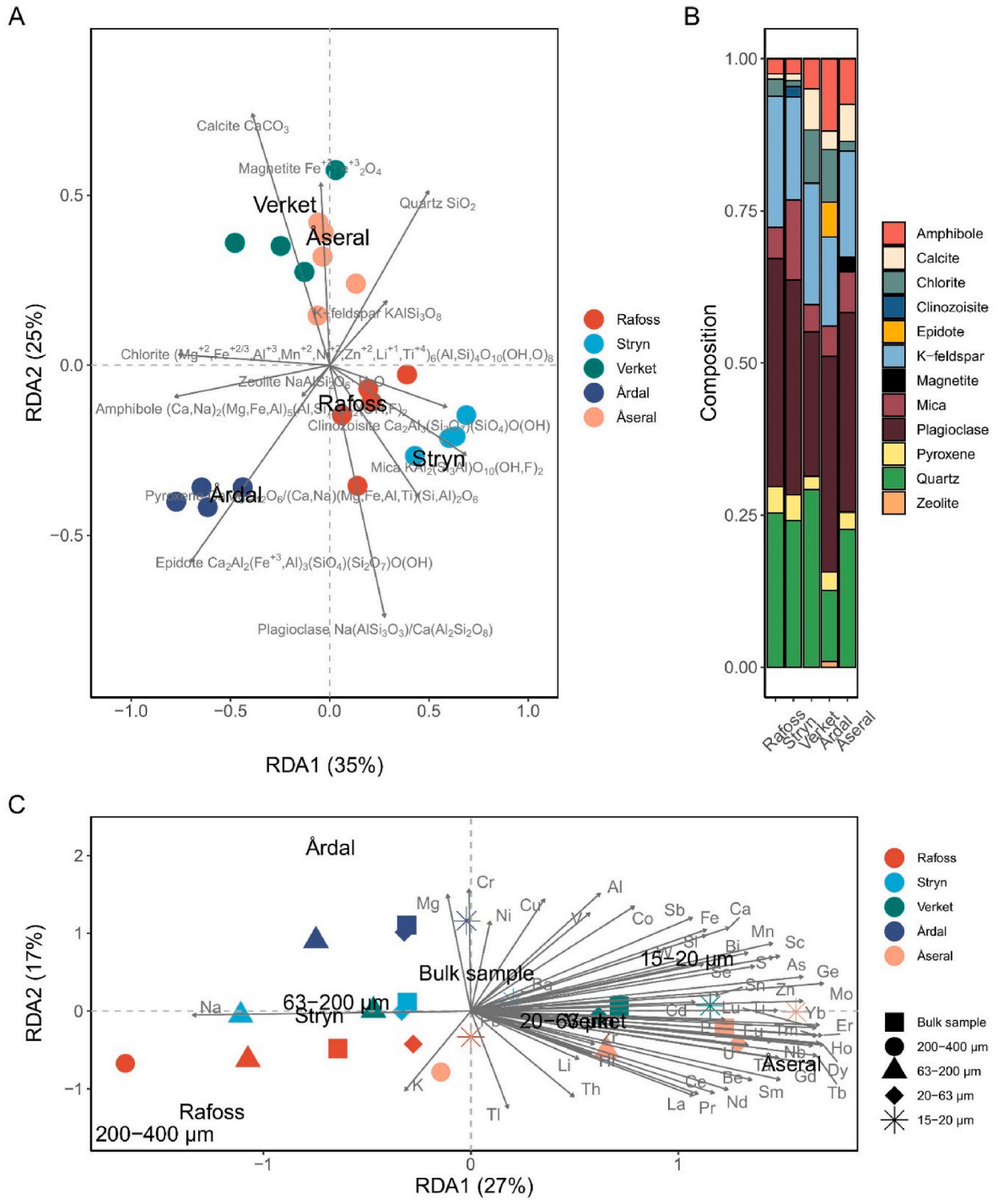

Fig. 3. (A) Partial RDA based on centered log-ratio transformed mineral compositions (including chemical formula; shown as grey vectors) in slurry samples and significant explanatory variable location (grey centroids) with size fractions as covariable. Minerals (black) are shown as vectors. Each point represents one individual sample (n = 22). (B) Bar plot of average mineral compositions in slurry samples (n = 22). (C) RDA based on log transformed (log 10 (x+1) element concentrations (shown as grey vectors) in slurry samples with significant explanatory variables location and size fractions shown as black centroids. Color indicates location (red = Rafoss, light blue = Stryn, green = Verket, dark blue = Årdal, beige = Åseral) and shape (square = Bulk sample, dot = 200–400 µm, triangle = 63–200 µm, diamond = 20–63 µm, star = 15–63 µm) indicate size fraction. Each point represents one individual sample (n = 22).

and 0.86–0.89 (±0.06–0.11), respectively. In contrast, NE particles were less "Elongated & Smooth" (37%) and more "Circular and Smooth" (38%) and AR and SLD overlapped between locations (0.67–0.68 (±0.13–0.14) and 0.87–0.88 (±0.071–0.075) respectively; Fig. SI-A Fig. 4A–B; SI-A Tables S8 and S10). Furthermore, tunnelling locations had higher fiber content, ranging from 3.4% (Årdal) to 5.6% (Åseral), than NE particles 1.1–2% (SI-A Fig. S9C & Table S8).

AR were significantly different between all locations (ANOVA $p < 0.001$, Tukey's HSD post-hoc test all $p < 0.008$; n = 740,103), except between NE particles (Vikka, Ravinebekken Oct and Nov: $p > 0.05$). SLD was also significantly different between locations (ANOVA $p < 0.001$, Tukey's HSD post-hoc test, n = 740,103), but with more variable results (SI-A Table S11). The largest morphological differences found for AR were between DB and NE particles. AR summary statistics (including

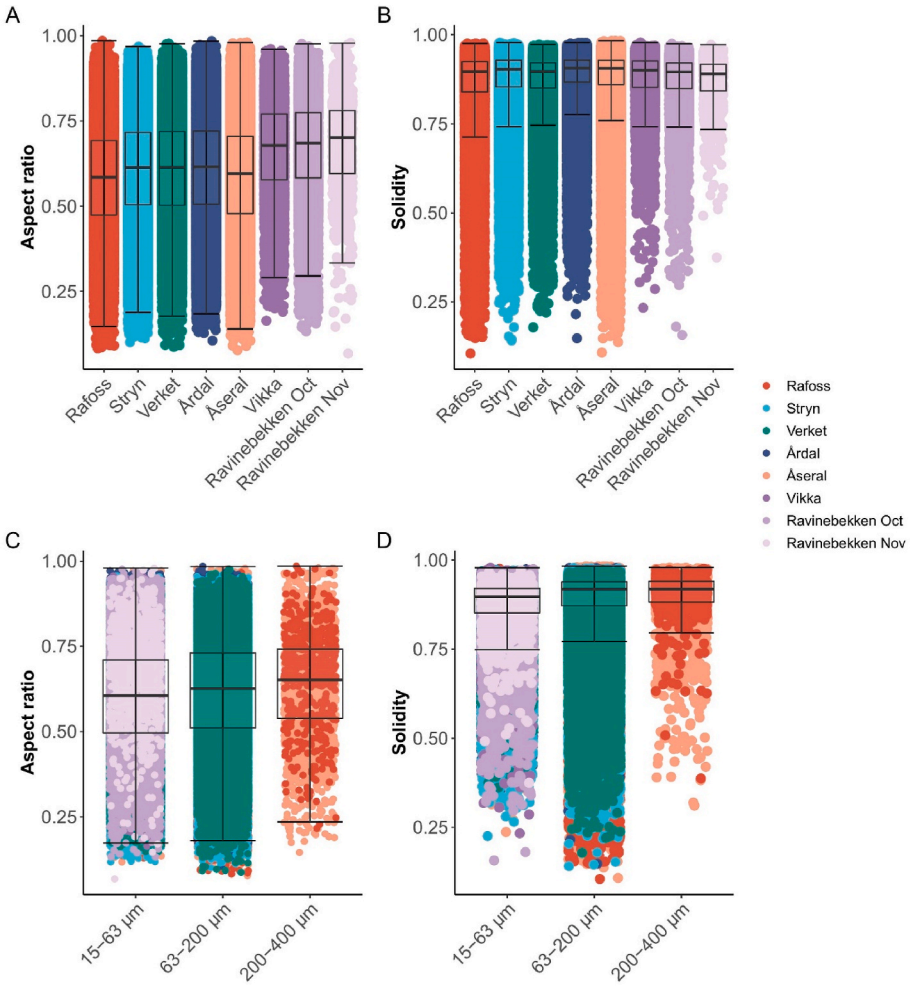

Fig. 4. Box plots of aspect ratio (A, C) and solidity (B, D) of tunnelling (Rafoss, Stryn, Verket, Årdal, Åseral) and naturally eroded (Vikka, Ravinebekken Oct and Nov) particles measured by Dynamic Image Analysis (DIA) sorted into location and size fractions (n = 740,103). Color indicates location (red = Rafoss, light blue = Stryn, green = Verket, dark blue = Årdal, beige = Åseral, dark purple = Vikka, medium purple = Ravinebekken Oct, light purple = Ravinebekken Nov). Box plots show the five-number summary of a set of data: including the minimum score, first (lower) quartile, median, third (upper) quartile, and maximum score.

mean, median, first and third quartile) were 8–15% lower for DB than NE particles, whereas SLD summary statistics only differed 0.3–0.8% (Fig. 4A–B; SI-A Table S8).

AR and SLD of DB particles increased slightly with increasing size fractions and were significantly different between all size fractions (AR: ANOVA $p < 0.001$, Tukey's HSD post-hoc test all $p < 0.0001$; SLD: Kruskal-Wallis rank sum test $p < 0.001$, Dunn post-hoc test with Bonferroni correction all $p < 0.001$; $n = 711{,}263$). However, the differences were small, and AR and SLD varied only 3% and 0.8% from the group means, respectively (Fig. 4C and D, SI-A Table S8).

Among the elements from ICP-MS, Be, Eu, Fe, Cr, Mg, Nb, Ni, Sb, Sm, Ta, U, V, Ti, P and Sn were significant in explaining the constrained variance in the RDA with DIA data, but only 2.1% of the variance was explained ($R^2adj = 0.02$, $p = 0.001$, $n = 711{,}263$; Fig. 5A). As for the minerals, all were significant in the RDA with DIA data, but they only explained 2% of the constrained variance ($R^2adj = 0.02$, $p = 0.001$; Fig. 5B). Despite being significant, all element and mineral trends were extremely modest, as also shown in Fig. 5A and B and further illustrated with a correlation (Pearson) heat plot (SI-A Figs. S9A–B), with coefficients falling between −0.08 and 0.1.

AR and SLD of DB particles from SIA and DIA were slightly different (SI-A Fig. S10), where the AR and SLD summary statistics differed 1–5% and 4–6%, respectively, between the two methods.

4. Discussion

4.1. How geochemical characteristics affect the morphology of DB particles

4.1.1. Mineral compositions and element concentrations

The prevailing minerals at all locations were the most dominant rock-forming silicate minerals in the Earth's crust, namely quartz, K-feldspar, and plagioclase (Singh et al., 2014). This indicates that all tunnelling locations mainly contained gneiss and granite igneous rock (granite-gneiss terrains), in agreement with prior geological surveys from these locations (Falkum, 1982; Heyer et al., 2001; Koestler, 1989; Lutro, 2003; NGU, 2022). Still, a variety of differences in mineral composition was observed among the locations, including higher relative contributions of the potential fiber-producing mineral groups amphibole at Verket, Årdal and Åseral and pyroxene at Rafoss and Stryn.

The major elements identified by ICP-MS were also, as anticipated, the most abundant elements in the Earth's crust (Singh et al., 2014; Yaroshevsky, 2006). Additionally, major elements agreed with the mineralogy results from the current study, where the three dominant rock-forming silicate minerals consist completely of Al, Ca, K, Na and Si (and O). Furthermore, the pattern of variation summarized in the ordinations of mineralogy and element concentration datasets, grouped the locations similarly. Thus, both mineral and elemental analyses identified the same differences and similarities among locations.

In contrast to mineralogy, increasing size fractions exhibited declining concentrations for all elements (except for Li, Na, K, Cd and Tl), a typical pattern seen in other study areas as well (e.g., pollution

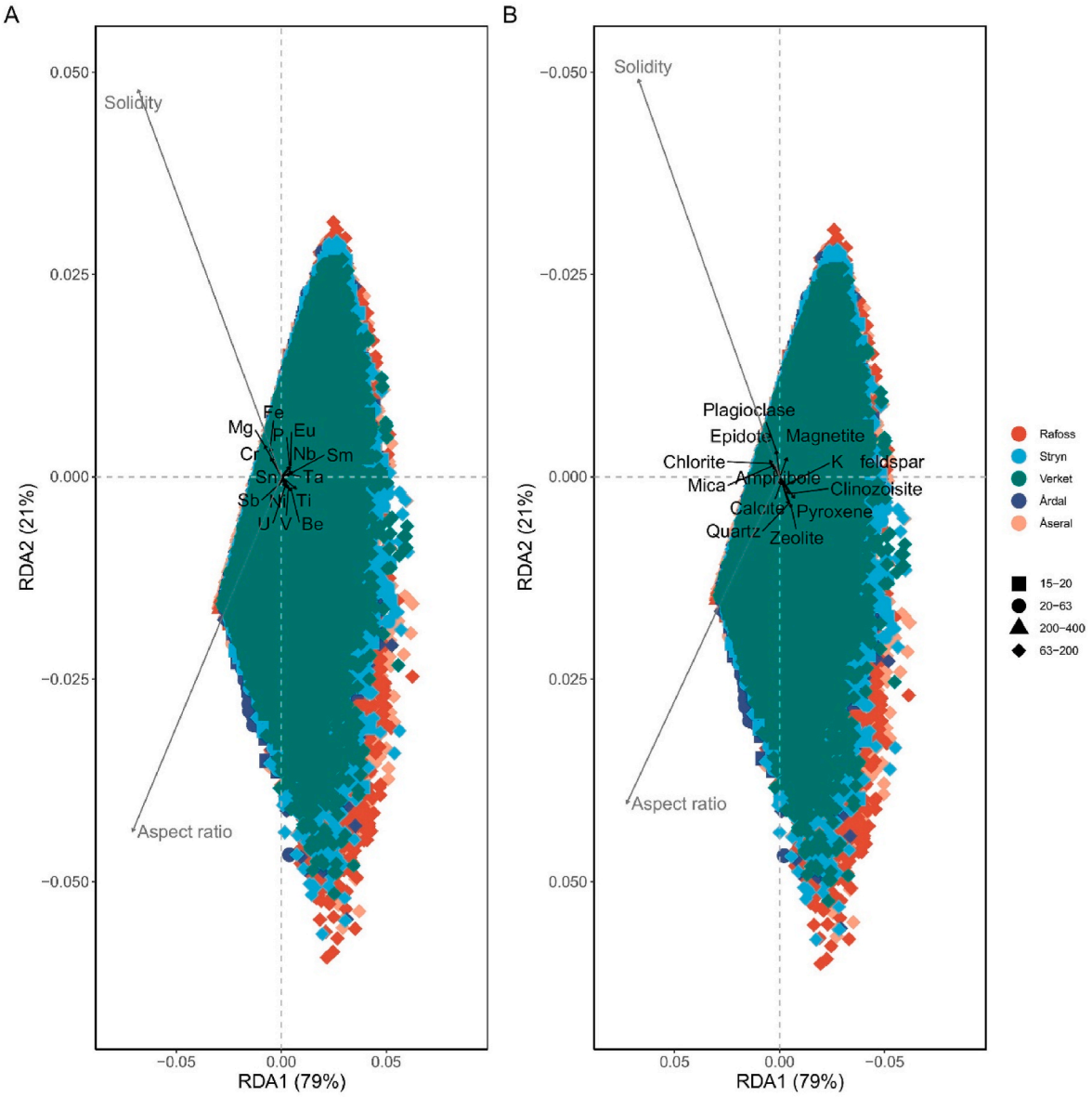

Fig. 5. (A) RDA based on morphology parameters aspect ratio and solidity of particles measured by Dynamic Image Analysis (DIA) and significant explanatory variables Be, Eu, Fe, Cr, Mg, Nb, Ni, Sb, Sm, Ta, U, V, Ti, P and Sn are shown as black vectors (n = 711,263). Each point represents one individual particle. (B) RDA based on morphology parameters aspect ratio and solidity of particles measured by DIA and significant explanatory variables of amphibole, calcite, chlorite, clinozoisite, epidote, k-feldspar, magnetite, mica, plagioclase, pyroxene, quartz, and zeolite are shown as black vectors (n = 711,263). Color indicates location (red = Rafoss, light blue = Stryn, green = Verket, dark blue = Årdal, beige = Åseral) and shape (square = 200–400 μm, dot = 63–200 μm, triangle = 20–63 μm, diamond = 15–20 μm) indicate size fraction.

from road surfaces (Jeong and Ra, 2022), mining (Li et al., 2014)). This pattern is typically attributed to higher surface area per unit weight exposing more surface to water and air which enhances weathering and surface-binding potential (Qian et al., 1996; Rodriguez-Rubio et al., 2003).

4.1.2. Size and morphology

Despite significant results for both mineral composition and element concentrations in explaining form and angularity of DB particles from DIA, extremely little of the variance was explained. Therefore, neither mineralogy nor elemental concentrations influenced DB particle morphology from granite-gneiss terrains. This contradicts the hypothesis that underlying geochemical characteristics affect the morphology of DB particles. In fact, both form and angularity of DB particles from DIA were very similar between tunnelling locations and the significant differences found in statistical testing between locations in morphology are attributed to high sample number (>700,000). This suggests that blasting and drilling influence DB particle morphology more than the underlying bedrock within the current geochemical characteristics of the study; granite-gneiss terrains. This is in line with a recent study of mine tailings, where particles were comparably angular, despite being geochemically different (Yang et al., 2019). However, despite finding significant differences in mineralogy and elemental content between tunnel locations in the present study, all the locations have comparable content of quartz, K-feldspar, and plagioclase, which make up the majority of the samples. This lack of geological variation could also explain why these tunnel construction locations produce similar particle morphology. For instance, different mineral fillers with more variable mineralogy than the current study, produced morphologically different particles (Xing et al., 2021).

Furthermore, another particle morphology study from mineral processing found mineral-specific morphologies of particles when

evaluating morphology and mineral composition of individual particles consisting of single minerals (Little et al., 2015). However, no element-specific morphology of individual particles from SIA were found in the present study. While this could be a result of low sample size (Leibrandt and Le Pennec, 2015; Liu et al., 2015) in the present study (n = 222 in SIA), it is also likely that minerals, which have specific crystalline structures, hardness, and other rock mass properties, and not individual elements, produce a particular morphology. Thus, future analysis of DB particles should further explore mineral-specific morphologies of individual particles and incorporate more variable mineralogy among samples than in the present study, including pure mineral samples, for further examination of how geology affect particle morphology in tunnelling.

Particle size distributions (laser diffraction) showed comparable results among the tunnelling locations, where most particles were silt and clay, and almost half the particles were under 10 μm. In the present study, both form and angularity exhibited a small decreasing trend with decreasing size fractions. This has previously been shown for form of ground cement particles (Holzer et al., 2010) and crushed bedrock aggregates (Cepuritis et al., 2014). Though the cause of this pattern is not known, Holzer et al. (2010) suggested that smaller particles formed during grinding, may be "clipped" from the surface of larger particles, possibly resulting in more elongated particles.

4.1.3. Comparing SIA and DIA imaging results

In the present study, DIA and SIA investigated particles from the same tunnelling slurries. Using both methods together bridge the advantages and shortcoming of each method (discussed in SI–B).

In the current study, both methods provided relatively similar AR and SLD results with only a few discrepancies. For example, form was slightly higher for SIA particles. This could be a result of filtering or sprinkling SIA-particles on a flat surface, which may result in a biased orientation towards the most stable position (longest axis; Liu et al., 2015), while DIA-particles are imaged in random orientations. Additionally, angularity was slightly lower for SIA-particles, which is consistent with other studies comparing the methods (Liu et al., 2015). This could be explained both by the higher average pixel density in SIA than in DIA and that blurring of the particle outline cause a smoothing effect (Liu et al., 2015; Sun et al., 2019a). In addition freeze-drying and ultrasonication of SIA-particles may alter the particles, which should be tested in the future. Furthermore, applicable to both form and angularity, differences in sample number and the low sample number in SIA (Leibrandt and Le Pennec, 2015; Liu et al., 2015), could have led to a biased sub-sampling of SIA-particles.

4.2. Morphological differences between DB and NE particles

In the present study, a significant difference was found for form and angularity between tunnelling locations and river sediment. However, the significant differences found are likely a result of the high sample number. Thus, it is more useful to look at gradients for comparison (Little et al., 2015). The differences between all summary metrics were very small comparing the tunnelling locations. However, comparing DB and NE particles showed a large difference in form. DB particles were more elongated and contained slightly higher fiber content, while NE particles were more circular. However, both particle types had similar angularity. These results partly supported the hypothesis that DB particles are more elongated and angular than NE particles. Form values of NE particles from the present study are in line with measurements of natural particles from Chinese aeolian sediments within the same size fraction (Shang et al., 2018). However, the greater elongation of DB particles compared with NE particles, is inconsistent with Cepuritis et al. (2014), which found that sand from a natural quarry deposit was more elongated than crushed and ground limestone (mostly calcite). Calcite is a mineral which exhibits three perfect cleavage direction at high angle to one another. Hence, crushing of pure calcite leads to formation of small particles with high aspect ratios, being a likely explanation for low degree of elongation for calcite-rich rocks such as limestone. Additionally, a study on angularity found that natural particles were consistently less angular than mine tailings, in contrast to the current study (Yang et al., 2019). These morphological disagreements between studies are likely attributed to differences in erosion history of NE particles, mineralogy and textural properties, which varies by location. Thus, this shows the importance of including references samples in morphological studies for comparison reasons.

There exist only a few, older studies on the toxicity of elongated particles (e.g., asbestos, splinters) in aquatic biota and these indicate that elongated particles may pose increased toxicity (Belanger et al., 1986a, 1986b; Belanger et al., 1986; Rodgers, 1969). Thus, DB particles from gneiss-granite which are more elongated than NE particles could potentially result in greater harm to aquatic biota when these particles are released into the environment.

5. Conclusions

To the best of our knowledge, this is the first quantitative (n > 700,000) morphological comparison between particles (61–91% < 63 μm) with different mineralogy from various tunnelling locations, against a reference particle; natural river sediments and water. Various methods such as DIA, SIA (ESEM-EDX, SM), laser diffraction, ICP-MS, μXRF and XRD were used in the current study to investigate how DB and NE particles diverge in morphology and how particle morphology is affected by the mineral and elemental characteristics. Results reveal that 1) DB particles were more elongated (lower aspect ratio) and contained slightly higher fiber content than NE particles, however 2) both particle types were comparably angular (similar solidity). Despite finding differences in geochemical attributes of the tunnelling slurries, they all originated from granite-gneiss terrains, and multivariate analysis showed that neither mineral nor elemental content affected the morphology of DB particles. This suggests that tunnelling activities are more influential than mineralogy working in granite-gneiss terrains, with respect to particle morphology.

Credit author statement

Emelie Skogsberg: conceptualization, methodology, formal analysis, investigation, writing – original draft, writing – reviewing and editing, visualization. *Lene Sørlie Heier*: initial conceptualization, resources, supervision, writing – review & editing. *Hans-Christian Teien*: initial conceptualization, methodology, supervision, writing – review & editing. *Ole Christian Lind*: initial conceptualization, methodology, investigation, writing – review & editing. *Per Hagelia*: methodology, writing – review & editing. *Sondre Meland*: initial conceptualization, methodology, supervision, project administration, funding acquisition, investigation, writing – review & editing.

Declaration of competing interest

The authors declare that they have no known competing financial interests or personal relationships that could have appeared to influence the work reported in this paper.

Data availability

Data will be made available on request.

Acknowledgements

Authors thank Karl Andreas Jenssen for ICP-MS analysis, Yetneberk Ayalew Kassaye for μXRF analysis, Hilde Rånås Kolstad for assistance with ESEM-EDX and The Norwegian Water Resources and Energy Directorate for collecting samples from Ravinebekken and morphology

analysis of these samples. Additionally, authors heartily thank Maeve McGovern and Jacqueline Knutson for proofreading the article. Authors gratefully acknowledge financial support from Norwegian Institute for Water Research and Norwegian Public Roads Administration. Additionally, part of the work is also supported by the Center for Environmental Radioactivity (CERAD) through the Norwegian Research Council's Centres of Excellence funding scheme (project number 223268/F50).

Appendix A. Supplementary data

Supplementary data to this article can be found online at https://doi.org/10.1016/j.envres.2023.116250.

References

Aitchison, J., 1986. The Statistical Analysis of Compositional Data. Chapman & Hall. https://doi.org/10.1002/bimj.4710300705.
Aitchison, J., Greenacre, M., 2002. Biplots of compositional data. J. Roy. Stat. Soc.: Series C (Applied Statistics) 51 (4), 375–392. https://doi.org/10.1111/1467-9876.00275.
Åkesson, U., Lindqvist, J., Göransson, M., Stigh, J., 2001. Relationship between texture and mechanical properties of granites, central Sweden, by use of image-analysing techniques. Bull. Eng. Geol. Environ. 60 (4), 277–284. https://doi.org/10.1007/s100640100105.
Altuhafi, F., O'Sullivan, C., Cavarretta, I., 2013. Analysis of an image-based method to quantify the size and shape of sand particles. J. Geotech. Geoenviron. Eng. 139, 1290–1307. https://doi.org/10.1061/(ASCE)GT.1943-5606.0000855.
Angermeier, P.L., Wheeler, A.P., Rosenberger, A.E., 2004. A conceptual framework for assessing impacts of roads on aquatic biota. Fisheries 29 (12), 19. https://doi.org/10.1577/1548-8446(2004)29[19. :ACFFAI]2.0.CO2.
Åstebøl, S.O., Hvitved-Jacobsen, T., Kjølholt, J., 2011. NORWAT - Nordic Road Water. Road and Water Pollution (46. Norweigian Public Roads Administration (in Norwegian).
Baccarelli, A., Pfeiffer, R., Consonni, D., Pesatori, A.C., Bonzini, M., Patterson, D.G., Landi, M.T., 2005. Handling of dioxin measurement data in the presence of non-detectable values: overview of available methods and their application in the Seveso chloracne study. Chemosphere 60 (7), 898–906. https://doi.org/10.1016/j.chemosphere.2005.01.055.
Barrett, P.J., 1981. Shape of rock particles, a critical review. Int. J. Rock Mech. Min. Sci. Geomech. Abstracts 18 (1), 2. https://doi.org/10.1016/0148-9062(81)90295-3.
Belanger, E.S., Schurr, K., Delmas, J.A., Gohara, A.F., 1986. Effects of chrysotile asbestos on coho salmon and green sunfish: evidence of behavioral and pathological stress. Environ. Res. 39, 74–85. https://doi.org/10.1016/S0013-9351(86)80009-3.
Belanger, E.S., Cherry, S.D., Cairns, J., 1986a. Seasonal, behavioral and growth changes of juvenile Corbicula Fluminea exposed to chrysotile asbestos. Water Res. 10, 1243–1250. https://doi.org/10.1016/0043-1354(86)90153-3.
Belanger, E.S., Cherry, S.D., Cairns, J., 1986b. Uptake of chrysotile asbestos fibers alters growth and reproduction of asiatic clams. Can. J. Fish. Aquat. Sci. 43, 43–52. https://doi.org/10.1139/f86-006.
Blanchet, F.G., Legendre, P., Borcard, D., 2008. Forward selection of explanatory variables. Ecology 89 (9), 2623–2632. https://doi.org/10.1890/07-0986.1.
Cepuritis, R., Wigum, B.J., Garboczi, E.J., Mørtsell, E., Jacobsen, S., 2014. Filler from crushed aggregate for concrete: pore structure, specific surface, particle shape and size distribution. Cement Concr. Compos. 54, 2–16. https://doi.org/10.1016/j.cemconcomp.2014.03.010.
Cioni, R., Pistolesi, M., Bertagnini, A., Bonadonna, C., Hoskuldsson, A., Scateni, B., 2014. Insights into the dynamics and evolution of the 2010 Eyjafjallajökull summit eruption (Iceland) provided by volcanic ash textures. Earth Planet Sci. Lett. 394, 111–123. https://doi.org/10.1016/j.epsl.2014.02.051.
Falkum, T., 1982. Geologisk Kart over Norge, Berggrunnskart MANDAL 1:250 000. Geology Survey of Norway (in Norwegian).
Gagnon, V., Rodrigue-Morin, M., Tremblay, J., Wasserscheid, J., Champagne, J., Bellenger, J.-P., Roy, S., 2020. Life in mine tailings: microbial population structure across the bulk soil, rhizosphere, and roots of boreal species colonizing mine tailings in northwestern Québec. Ann. Microbiol. 70 (1), 1–18. https://doi.org/10.1186/s13213-020-01582-9.
Greenacre, M., 2018. Compositional Data Analysis in Practice. Chapman & Hall/CRC.
Gualtieri, A.F., 2020. Naturally occurring asbestos: a global health concern? State of the art and open issues. Environ. Eng. Geosci. 26 (1), 3–8. https://doi.org/10.2113/EEG-2271.
Hessen, D., Bjerknes, V., Bækken, T., Aanes, J.K., 1989. Økt Slamføring I Vetlefjordselva Som Følge Av Anleggsarbeid. Effekter På Fisk Og Bunndyr (0-88016. Norwegian Institute for Water Research (in Norwegian).
Heyer, H., Bøe, R., Hageskov, B., Lutro, O., 2001. Berggrunnskart; horten. 000; Foreløpig utgave plotteversjon. Geology Survey of Norway 1 (50), 18131 (in Norwegian).
Hindar, A., Nordstrom, D.K., 2015. Effects and quantification of acid runoff from sulfide-bearing rock deposited during construction of Highway E18, Norway. Appl. Geochem. 62, 150–163. https://doi.org/10.1016/j.apgeochem.2014.06.016.
Hjulstad, M., 2015. Leaching, Uptake and Effects in Brown Trout (Salmo trutta) of Radionuclides and Metals from Black Shales and Sulphur Bearing Gneiss. Norwegian University of Life Sciences (NMBU), Ås, Norway (Master Thesis (MSc)).
Holzer, L., Flatt, R., Erdoğan, S., Bullard, J., Garboczi, E.J., 2010. Shape comparison between 0.4–2.0 and 20–60 μm cement particles. J. Am. Ceram. Soc. 93, 1626–1633. https://doi.org/10.1111/j.1551-2916.2010.03654.x.
Jacobsen, P., Grande, M., Aanes, K.J., Kristiansen, H., Andersen, S., 1987. Vudering Av Årsaker Til Fiskedød Ved G.P. Jægtvik A.S., Langstein. Norwegian Institute for Water Research (in Norwegian).
Jeong, H., Ra, K., 2022. Source apportionment and health risk assessment for potentially toxic elements in size-fractionated road dust in Busan Metropolitan City, Korea. Environ. Monit. Assess. 194 (5), 350. https://doi.org/10.1007/s10661-022-10008-9.
Kaegi, R., 2004. Chemical and morphological analysis of airborne particles at a tunnel construction site. J. Aerosol Sci. 35 (5), 621–632. https://doi.org/10.1016/j.jaerosci.2003.11.001.
Kettler, T.A., Doran, J.W., Gilbert, T.L., 2001. Simplified method for soil particle-size determination to accompany soil-quality analyses. Soil Sci. Soc. Am. J. 65 (3), 849–852. https://doi.org/10.2136/sssaj2001.653849x.
Koestler, A.G., 1989. Hurrungane. Berggrunnskart; hurrungane. 000; trykt i farger. Geology Survey of Norway 1 (50), 15174 (in Norwegian).
Leibrandt, S., Le Pennec, J.-L., 2015. Towards fast and routine analyses of volcanic ash morphometry for eruption surveillance applications. J. Volcanol. Geoth. Res. 297, 11–27. https://doi.org/10.1016/j.jvolgeores.2015.03.014.
Li, Q., Ji, H., Qin, F., Tang, L., Guo, X., Feng, J., 2014. Sources and the distribution of heavy metals in the particle size of soil polluted by gold mining upstream of Miyun Reservoir, Beijing: implications for assessing the potential risks. Environ. Monit. Assess. 186 (10), 6605–6626. https://doi.org/10.1007/s10661-014-3877-4.
Little, L., Becker, M., Wiese, J., Mainza, A.N., 2015. Auto-SEM particle shape characterisation: investigating fine grinding of UG2 ore. Miner. Eng. 82, 92–100. https://doi.org/10.1016/j.mineng.2015.03.021.
Liu, E.J., Cashman, K.V., Rust, A.C., 2015. Optimising shape analysis to quantify volcanic ash morphology. GeoResJ 8, 14–30. https://doi.org/10.1016/j.grj.2015.09.001.
Lois-Morales, P., Evans, C., Weatherley, D., 2022. Analysis of the size–dependency of relevant mineralogical and textural characteristics to particles strength. Miner. Eng. 184, 107572 https://doi.org/10.1016/j.mineng.2022.107572.
Lubbe, S., Filzmoser, P., Templ, M., 2021. Comparison of zero replacement strategies for compositional data with large numbers of zeros. Chemometr. Intell. Lab. Syst. 210, 104248 https://doi.org/10.1016/j.chemolab.2021.104248.
Lundy, L., Revitt, M., Ellis, B., 2016. D4.1 Literature Review on Treatment of Runoff from Highway Construction Site. Conference of European Directors of Roads.
Lutro, O., 2003. Stryn. Berggrunnskart; Stryn. 000; Foreløpig utgåve plotteversjon. Geology Survey of Norway 1 (50), 13181 (in Norwegian).
Maroof, M.A., Mahboubi, A., Noorzad, A., Safi, Y., 2020. A new approach to particle shape classification of granular materials. Transportation Geotechnics 22, 100296. https://doi.org/10.1016/j.trgeo.2019.100296.
Mazzoli, A., Favoni, O., 2012. Particle size, size distribution and morphological evaluation of airborne dust particles of diverse woods by Scanning Electron Microscopy and image processing program. Powder Technol. 225, 65–71. https://doi.org/10.1016/j.powtec.2012.03.033.
Mazzoli, A., Moriconi, G., 2014. Particle size, size distribution and morphological evaluation of glass fiber reinforced plastic (GRP) industrial by-product. Micron 67, 169–178. https://doi.org/10.1016/j.micron.2014.07.007.
Meijer, J.R., Huijbregts, M.A.J., Schotten, K.C.G.J., Schipper, A.M., 2018. Global patterns of current and future road infrastructure. Environ. Res. Lett. 13 (6), 1–11. https://doi.org/10.1088/1748-9326/aabd42.
Mooselu, M.G., Amiri, H., Azadi, S., Liltved, H., 2022. Spatiotemporal assessment of surface water vulnerability to road construction. Environ. Dev. Sustain. 24 (6), 7851–7873. https://doi.org/10.1007/s10668-021-01763-9.
Newbury, D.E., Ritchie, N.W.M., 2013. Is scanning electron microscopy/energy dispersive X-ray spectrometry (SEM/EDS) quantitative? Scanning 35 (3), 141–168. https://doi.org/10.1002/sca.21041.
NGU, 2022. Berggrunn - Nasjonal Berggrunnsdatabase. Geology Survey of Norway (in Norwegian).
Oksanen, J., Blanchet, F.G., Friendly, M., Kindt, R., Legendre, P., McGlinn, D., Wagner, H., 2017. Vegan: Community Ecology Package.
Pabst, T., Hindar, A., Hale, S., Garmo, Ø., Endre, E., Petersen, K., Baardvik, G., 2015. The Potential Impact of Various Rock Types on the Aquatic Environment during Building and Construction Projects, vol. 389. Norwegian Public Roads Administration.
Palarea-Albaladejo, J., Martín-Fernández, J.A., 2015. zCompositions — R package for multivariate imputation of left-censored data under a compositional approach. Chemometr. Intell. Lab. Syst. 143, 85–96. https://doi.org/10.1016/j.chemolab.2015.02.019.
Pawlowsky-Glahn, V., Buccianti, A., 2011. Compositional Data Analysis: Theory and Applications. Wiley. https://doi.org/10.1002/9781119976462.ch17.
Pye, K., Blott, S.J., 2004. Particle size analysis of sediments, soils and related particulate materials for forensic purposes using laser granulometry. Forensic Sci. Int. 144 (1), 19–27. https://doi.org/10.1016/j.forsciint.2004.02.028.
Qian, J., Shan, X.-q., Wang, Z.-j., Tu, Q., 1996. Distribution and plant availability of heavy metals in different particle-size fractions of soil. Sci. Total Environ. 187 (2), 131–141. https://doi.org/10.1016/0048-9697(96)05134-0.
Quinn, T.P., Erb, I., Gloor, G., Notredame, C., Richardson, M.F., Crowley, T.M., 2019. A field guide for the compositional analysis of any-omics data. GigaScience 8 (9), giz107. https://doi.org/10.1093/gigascience/giz107.
R Core Team, 2021. R: A Language and Environment for Statistical Computing. R Foundation for Statistical Computing, Vienna, Austria. URL. https://www.R-project.org/.
Rietveld, H.M., 2014. The Rietveld method. Phys. Scripta 89 (9), 098002. https://doi.org/10.1088/0031-8949/89/9/098002.

Rodgers, A.B., 1969. Tolerance Levels of Four Species of Estaurine Fishes to Suspended Mineral Solids. University of Rhode Island, Rhode Island.

Rodriguez-Rubio, P., Morillo, E., Madrid, L., Undabeytia, T., Maqueda, C., 2003. Retention of copper by a calcareous soil and its textural fractions: influence of amendment with two agroindustrial residues. Eur. J. Soil Sci. 54 (2), 401–409. https://doi.org/10.1046/j.1365-2389.2003.00529.x.

Roseth, R., Sørlie Heier, L., Heggland, A., Preus Hveding, Ø., Skrutvold, J., Rognan, Y., Kjerkol, H., 2021. Avrenning Av Partikler I Anleggsprosjekter; Betydning for Fisk Og Vannmiljø. Vann, p. 3 (in Norwegian).

Shang, Y., Kaakinen, A., Beets, C., Prins, M., 2017. Aeolian silt transport processes as fingerprinted by dynamic image analysis of the grain size and shape characteristics of Chinese loess and Red Clay deposits. Sediment. Geol. 375 https://doi.org/10.1016/j.sedgeo.2017.12.001.

Shang, Y., Kaakinen, A., Beets, C.J., Prins, M.A., 2018. Aeolian silt transport processes as fingerprinted by dynamic image analysis of the grain size and shape characteristics of Chinese loess and Red Clay deposits. Sediment. Geol. 375, 36–48. https://doi.org/10.1016/j.sedgeo.2017.12.001.

Singh, B., Cattle, S.R., Field, D.J., 2014. Edaphic soil science, introduction to. In: Van Alfen, N.K. (Ed.), Encyclopedia of Agriculture and Food Systems. Academic Press, Oxford, pp. 35–58. https://doi.org/10.1016/B978-0-444-52512-3.00092-9.

South, A., 2017. Rnaturalearth: World Map Data from Natural Earth. R package version 0.1.0. https://CRAN.R-project.org/package=rnaturalearth.

Sun, Q., Zheng, J., Coop, M.R., Altuhafi, F.N., 2019a. Minimum image quality for reliable optical characterizations of soil particle shapes. Comput. Geotech. 114, 103110 https://doi.org/10.1016/j.compgeo.2019.103110.

Sun, Y., Cai, Z., Fu, J., 2019b. Particle morphomics by high-throughput dynamic image analysis. Sci. Rep. 9 (1), 9591. https://doi.org/10.1038/s41598-019-46062-6.

Van den Boogaart, K.G., Tolosana-Delgado, R., 2013. Analyzing Compositional Data with R, 2013 ed. Springer Berlin/Heidelberg, Berlin, Heidelberg: Berlin, Heidelberg. https://doi.org/10.1007/978-3-642-36809-7.

Vikan, H., Meland, S., 2013. Purification practices of water runoff from construction of Norwegian tunnels- status and research gaps. In: Rauch, S., Morrison, G., Norra, S., Schleicher, N. (Eds.), Urban Environment. Springer. https://doi.org/10.1007/978-94-007-7756-9_42.

Wærsted, F.M., 2019. Mobility of Naturally Occurring Radionuclides and Stable Elements in Alum Shale: A Case Study of Gran, Highway 4, Norway. (Philosophiae Doctor (PhD)). Norwegian University of Life Sciences (NMBU), Ås, Norway.

Wheeler, S., Henry, T., Murray, J., McDermott, F., Morrison, L., 2021. Utilising CoDA methods for the spatio-temporal geochemical characterisation of groundwater; a case study from Lisheen Mine, south central Ireland. Appl. Geochem. 127, 104912 https://doi.org/10.1016/j.apgeochem.2021.104912.

Who, 1985. The WHO/EURO man-made mineral fiber reference scheme. Scand. J. Work. Environ. Health 11 (2), 123–129. https://doi.org/10.5271/sjweh.2251.

Xing, B., Fan, W., Lyu, Y., Sun, H., Che, J., 2021. Influence of particle mineralogy and size on the morphological characteristics of mineral fillers. J. Mater. Res. Technol. 15, 3995–4009. https://doi.org/10.1016/j.jmrt.2021.10.026.

Yang, Y., Wei, Z., Fourie, A., Chen, Y., Zheng, B., Wang, W., Zhuang, S., 2019. Particle shape analysis of tailings using digital image processing. Environ. Sci. Pollut. Control Ser. 26 (25), 26397–26403. https://doi.org/10.1007/s11356-019-05974-6.

Yaroshevsky, A.A., 2006. Abundances of chemical elements in the Earth's crust. Geochem. Int. 44 (1), 48–55. https://doi.org/10.1134/S001670290601006X.